UNIVERSIDADE FEDERAL DO RIO GRANDE DO SUL
INSTITUTO DE FÍSICA
DEPARTAMENTO DE FÍSICA

SUPERHYDROPHOBIC Pt-CeO_2 NANOPARTICLES AS EFFICIENT CATALYST FOR THE REVERSE WATER-GAS SHIFT REACTION

KAUÊ GIESE GOMES DOS SANTOS

PORTO ALEGRE, RS, BRAZIL
2023

UNIVERSIDADE FEDERAL DO RIO GRANDE DO SUL
INSTITUTO DE FÍSICA
DEPARTAMENTO DE FÍSICA

Nanopartículas de Pt-CeO_2 superhidrofóbicas como catalisador eficiente para a reação inversa de deslocamento gás-água

KAUÊ GIESE GOMES DOS SANTOS

Dissertação submetida como requerimento parcial
para obtenção do título de Mestre em Física

Orientador:
Fabiano Bernardi, Prof. Dr.

PORTO ALEGRE, RS
2023

ACKNOWLEDGEMENT

I thank my family for all the support they provided me during my formation. To my friends from both inside and outside the course for always being by my side. To my teachers, scholarship colleagues, and especially to my advisor Fabiano Bernardi for all the knowledge I gained during the beginning of my academic life.

I would also like to thank the LNLS, CNANO, LNNano, Laboratório Implantação Iônica and CMM laboratories and the research funding agencies, CAPES, CNPq, and FAPERGS for making this research possible.

Abstract

The excessive burning of fossil fuels like oil and coal increased the CO_2 concentration in the atmosphere and it currently exceeds 400 ppm. Consequently, the greenhouse effect increases the average Earth's temperature, rises of oceans level and impairs the biodiversity. Then it is needed an efficient way to dissociate the CO_2 molecule. A promising way to dissociate this molecule is through the RWGS (Reverse Water Gas-Shift) reaction. In this work, three different Pt-CeO_2 nanoparticles were synthesized and caracterized for application in the RWGS reaction, where one of them is superhydrophic. Superhydrophobic nanoparticles are expected to shift the RWGS reaction equilibrium towards the formation of CO products, thus increasing the dissociation efficiency of the CO_2 molecule. Initially, TEM and SAXS measurements were performed to determine the size distribution of the Pt commercial nanoparticles, obtaining an average diameter of 3 nm. The Pt concentration in each sample was found to be approximately 8 wt% by means of RBS measurements. The chemical components at the surface of the as-prepared samples were probed using XPS measurements. The surface of Pt nanoparticles are mainly formed by a Pt$(OH)_x$ component. After this, the Pt-CeO_2 samples were heated to 400 $^\circ C$ while exposed to a H_2 atmosphere to create oxygen vacancies before starting the RWGS reaction. During this process, the samples were characterized by the Mass Spectrometry, in situ time resolved XANES measurements at the Ce L_3 edge and in situ EXAFS measurements at the the Pt L_3 edge. It was observed an improved reactivity in the RWGS reaction for the superhydrophobic samples. The reactivity is directly proportional to the reducibility of CeO_2 or, in other words, to the oxygen vacancy population at the surface of CeO_2. The Pt nanoparticles were encapsulated by oxide moieties from the support during reduction treatment (Strong Metal-Support Interaction (SMSI)

effect) but, besides this, the nanoparticles remain active for the RWGS reaction. The superhydrophobic Pt-CeO_2 nanoparticles synthesized are promising for future applications in the RWGS reaction.

Keywords: Reverse Water Gas Shift reaction, Pt-CeO_2, global warming, oxygen vacancy

Resumo

A queima excessiva de combustíveis fósseis como o petróleo e o carvão aumentaram a concentração de CO_2 na atmosfera que atualmente excede 400 ppm. Consequentemente, o efeito estufa aumenta a temperatura média da Terra, eleva o nível dos oceanos e prejudica a biodiversidade. Portanto, é necessário um meio eficiente de dissociar a molécula de CO_2. Um caminho promissor para dissociar essa molécula é através da reação Inversa de Deslocamento Gás-Água (RWGS). Neste trabalho, foram sintetizadas e caracterizadas três diferentes nanopartículas de Pt-CeO_2 para aplicação na reação RWGS, sendo uma delas super-hidrofóbica. Espera-se que as nanopartículas super-hidrofóbicas desloquem o equilíbrio da reação RWGS para a formação de CO, aumentando assim a eficiência da dissociação da molécula de CO_2. Inicialmente, foram realizadas medidas de TEM e SAXS para determinar a distribuição de tamanho das nanopartículas comerciais de Pt, obtendo um diâmetro médio de 3 nm. A concentração de Pt em cada amostra foi de aproximadamente 8 wt%, conforme obtido por medidas de RBS. As componentes químicas na superfície das amostras como preparadas foram investigados usando medidas de XPS. A superfície das nanopartículas de Pt é principalmente composta por uma componente de $Pt(OH)_x$. Após, as amostras de Pt-CeO_2 foram aquecidas a 400 $^{\circ}C$ enquanto expostas a uma atmosfera redutora de H_2 para criar vacâncias de oxigênio antes de iniciar a reação RWGS. Durante esse processo, as amostras foram caracterizadas por Espectrometria de Massas, medidas de XANES in situ com resolução temporal na borda L_3 do Ce e medidas de EXAFS in situ na borda L_3 da Pt. Observou-se uma melhoria na reatividade na reação RWGS para as amostras super-hidrofóbicas. A reatividade é diretamente proporcional à capacidade de redução do suporte de CeO_2, ou seja, à população de vacâncias de oxigênio na superfície do suporte de CeO_2. As nanopartículas

de Pt foram encapsuladas por grupos de óxido do suporte durante o tratamento de redução (efeito de Interação Forte entre Metal-Suporte (SMSI)), mas, além disso, as nanopartículas continuam ativas para a reação de RWGS. As nanopartículas de Pt-CeO_2 super-hidrofóbicas sintetizadas são promissoras para futuras aplicações na reação RWGS.

Palavras-chave: reação Inversa de Deslocamento Gás-Água, Pt-CeO_2, Aquecimento global, Vacância de oxigênio

Contents

List of Figures

List of Tables

Chapter 1

Global warming and catalysts

In this chapter, fundamental themes associated with global warming will be addressed for the reader's understanding of the development of the work.

1.1 Introduction

Global warming is one of the most important issues of the modern world, that has captured the attention of cientists all over the world. It refers to the gradual increase in the Earth's average surface temperature due to the accumulation of greenhouse gases, such as CO_2, NO_x, water vapor and methane, in the atmosphere [1]. The solar energy (mainly IR) is reflected at the Earth's surface back to the atmosphere. The greenhouse gases absorb this radiation and emit it again in all directions, including back to the Earth's surface that increases its average temperature. Figure 1.1 illustrates a comparison of the phenomenon before and after human influence. It leads to a range of impacts such as the increase on infectious deseases, sea level rise and increase on natural disasters as hurricanes and heatwaves [2, 3, 4]. The issue of global warming has far-reaching implications for our planet and requires immediate attention and action to address its causes and mitigate its effects. The Paris Agreement is an international treaty aimed at combating climate change and its effects. It was adopted on December

12, 2015, at the 21st Conference of the Parties (COP21) of the United Nations Framework Convention on Climate Change (UNFCCC) held in Paris, France, where 196 parties have ratified the agreement. The agreement's objective is to limit global warming to well below 2 °C above pre-industrial levels and to pursue efforts to limit the temperature increase to 1.5 °C above pre-industrial levels [5].

Carbon dioxide (CO_2) is the primary greenhouse gas responsible for global warming. In fact, CO_2 is not the more efficient molecule for IR re-emission into Earth's surface but the large amount of CO_2 realeased nowadays makes it the great villain of global warming. Figure 1.2 shows a correlation between the rising leves of CO_2 in the atmosphere with the increase of the mean temperature in Earth's surface.

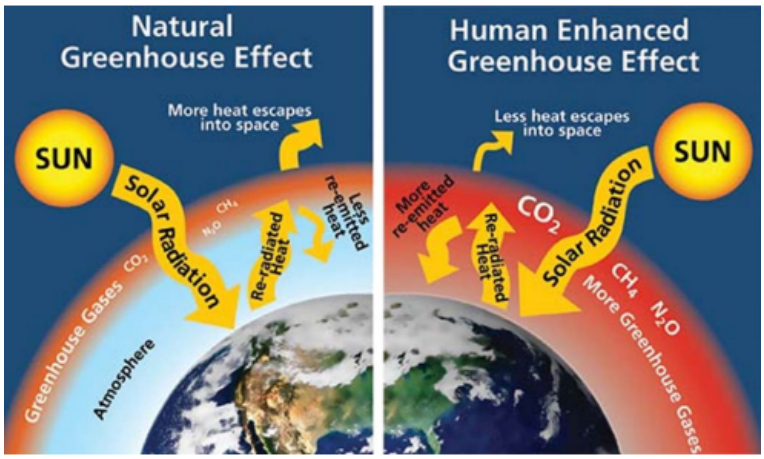

FIGURE 1.1. Illustration of greenhouse effect before and after human influence [6]

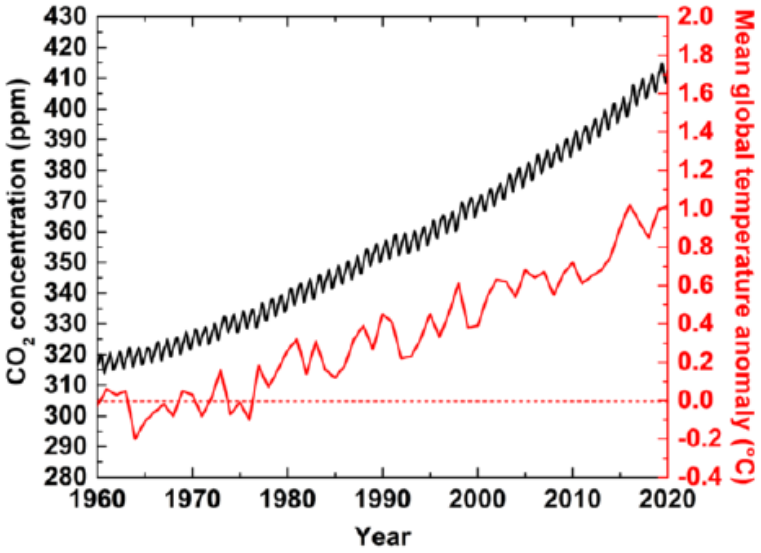

FIGURE 1.2. Comparison between the CO_2 concentration in the atmosphere and the mean global temperature anomaly in the past few decades [7].

CO_2 emissions come from various human activities such as burning fossil fuels, deforestation and industrial processes. The concentration of CO_2 in the atmosphere has been steadily increasing since the Industrial Revolution, and its concentration nowadays exceeds 400 ppm [1]. Mitigating the impacts of global warming requires a reduction in CO_2 emissions, which can be achieved through strategies such as decreasing fossil fuel consumption, carbon capture and storage and through the replacement of the current energy matrix by one based on to renewable energy sources. Besides the influence on the global warming, recently, CO_2 has been viewed as an abundant carbon source that can be used as a raw material for biofuels and useful chemicals like methanol and carbon monoxide, which can be used as raw material for plastic and medicine syntesis, and even as a replacement for oxygen in metal-air batteries [6, 8, 9].

The release of carbon dioxide (CO_2) during the combustion of fossil fuels is widely recognized as a significant contributor to global warming. Carbon Capture Utilization and Storage (CCUS) methods and technologies is a current way to reduce the CO_2 emission by capturing

the CO_2 molecule in three different ways: pre-combustion carbon capture, post-combustion carbon capture and the oxy-combustion carbon capture method [10]. A diagram explaining the methods and techniques for CO_2 capture is shown in Figure 1.3. Another effective way to deal with the rising levels of CO_2 in the atmosphere is transforming the CO_2 molecules into new compounds through the use of catalysts. Catalysts are materials that provide a different raection path for a given chemical reaction. A metal nanoparticle supported over a metal oxide is a typical catalyst type used for CO_2 dissociation. In particular, this type of catalyst is frequently used in chemical reations involving the combination of H_2 and CO_2 molecules. The resulting chemical products vary depending on the reaction conditions and catalysts used during the process. Some of these products are methanol (CH_3OH), formic acid ($HCOOH$), dimethyl ether (C_2H_6O), carbon monoxide (CO) and methane (CH_4). These chemicals can be used as fuel, antibacterial agent, refrigerant, raw material for the production of other chemicals, among others industrial process.

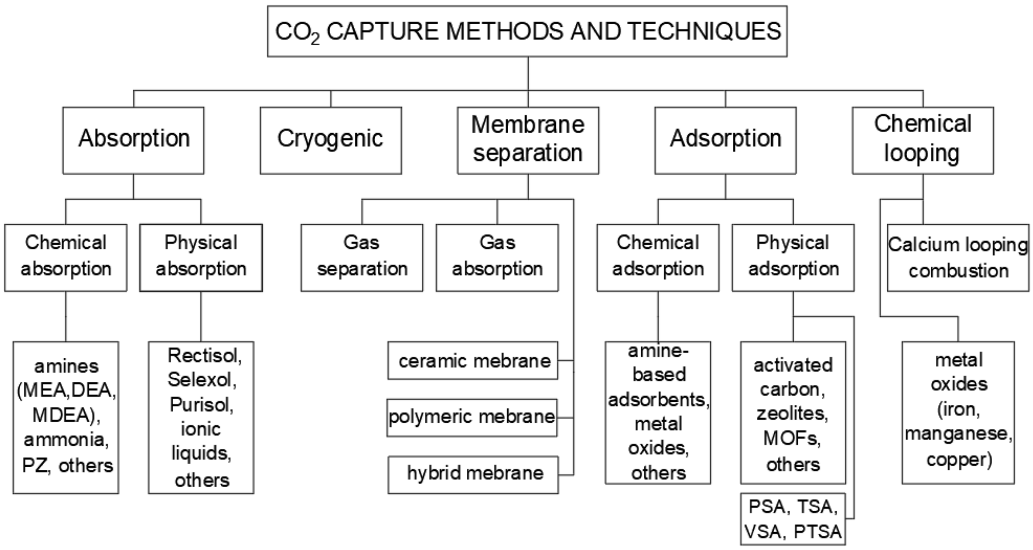

FIGURE 1.3. Methods and techniques used for CO_2 capture [10].

In the literature, several different catalysts are used for CO_2

dissociation. The majority of catalysts used for CO_2 dissociation present issues like poor CO_2 conversion rates, high operating temperatures, as well low selectivity. When a catalyst needs high temperatures for operation, a considerable amount of energy is expended to achieve the desired condition, resulting in the generation of excessive CO_2 and an unprofitable financial and environmental situation. Considering this, highly efficient catalysts for CO_2 dissociation operating at low temperatures need to be developed urgently.

1.2 Reverse Water Gas-Shift reaction (RWGS) as a promising solution

The Reverse Water Gas-Shift (RWGS) reaction is a widely studied process for the dissociation of CO_2. It consists on the chemical reaction between hydrogen gas and carbon dioxide, ultimately yielding carbon monoxide and water, represented by the equation below:

$$CO_2 + H_2 \rightleftarrows CO + H_2O \tag{1.1}$$

The CO produced is a poisonous gas that is colorless, odorless, and tasteless, often referred to as the silent killer. Despite its harmful effects, this molecule can be used as feedstock for renewable energy sources and as a raw material for various reactions, including the production of hydrocarbons, plastics, and other useful chemicals like methanol. The main obstacle in the RWGS reaction is that it is an endothermic process with a high enthalpy at room temperature and atmospheric pressure (+ 41.16 kJ/mol) [11]. To overcome this, catalysts are typically used to enhance the reaction rate. Current catalysts used for the RWGS reaction are made of metallic or bimetallic nanoparticles of Cu, Ni, and Pt suported on oxides like CeO_2, SiO_2, and Al_2O_3, which improve thermal stability of the nanoparticles [12, 13, 14].

Table 1.1 displays CO_2 conversion values for catalysts identified in literature for the RWGS reaction. CO_2 conversion rates are low and the reaction requires high temperatures for successful implementation, highlighting the need to improve current catalysts used in the RWGS reaction. Besides the high stability of the CO_2 molecule itself, some aditional issues arrive for CO_2 dissociation. Some problems faced by catalyst used in the RWGS reation are the sintering of the metallic nanoparticles (the aglomeration of metallic nanoparticles, leading to a reduced superficial area) due to the high temperature of the RWGS reaction, and carbon deposition on the surface, like soot, both of which promoting the catalyst deactivation.

TABLE 1.1. Comparison between the performance of catalysts found in literature for the RWGS reaction.

Material	Temperature (K)	Pressure (atm)	CO_2 conversion (%)	Reference
9% Cu/SiO_2	873	1	5.3	[15]
(9%Cu+1.9%K)/SiO_2	873	1	12.8	[15]
1 wt% Rh/SiO_2	473	50	52	[16]
$Mn/Fe/Al_2O_3$	563	13.8	38.6	[17]
Rh-Fe/TiO_2	543	20.26	9.16	[18]
NiO/SBA-15	673	1	5	[19]
Ni/CeO_2	1023	1	40	[20]
Co/β-Mo_2C	473	20	9	[22]
$PtCo/CeO_2$	573	1	6.6	[21]
2%Pt/CeO_2	498	1	13.7	[23]
Pt/CeO_2	573	1	10	[24]
Pt-CeO_2/Mesoporous SiO_2	673	1	20	[25]
Fe–Pt/CeO_2	623	1	21	[26]
Pt/CeO_2	623	1	14	[26]

Another issue faced by modern catalysts is the low selectivity, that is, the formation of subproducts different than those expected for RWGS reaction [27]. Additional byproducts include CH_4 coming from related reactions that may also occur like:

Methanation

$$CO + 3H_2 \rightleftarrows CH_4 + H_2O \qquad \Delta H^0_{298} = -206{,}5Kj/mol$$

and the Sabatier reaction

$$CO_2 + 4H_2 \rightleftarrows CH_4 + 2H_2O \qquad \Delta H^0_{298} = -165{,}0Kj/mol$$

In the past couple decades, Pt/CeO_2 catalysts have emerged as a promising catalyst for the RWGS reaction. These catalysts demonstrate high selectivity towards the RWGS reaction and are capable of operating effectively at atmospheric pressure and relatively low temperatures [23, 24, 25, 26].

1.3 Pt-CeO_2 catalysts in the RWGS reaction

In addition to its status as a noble metal, what makes the use of Pt very costly, Pt presents some desirable properties as catalysts for the RWGS reaction, such as its ability to dissociate hydrogen molecules and a low oxidation rate [28]. Cerium oxide is an oxide with a great ability to readily switch between the fully oxidized (Ce(IV), CeO_2) and fully reduced (Ce(III), Ce_2O_3) state. The reduction process of CeO_2 creates oxygen vacancies[29, 30], as illustrated in Figure 1.4, which are one of the most active sites for catalytic applications.

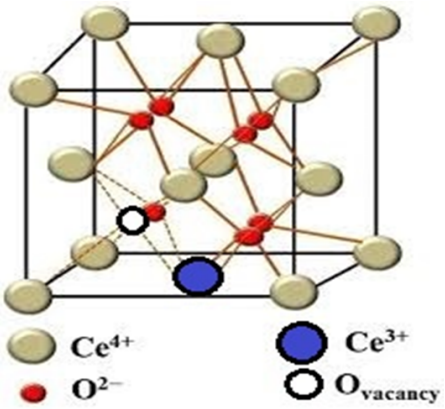

FIGURE 1.4. Squematic representation of an oxygen vacancy in the cerium oxide crystaline structure [31].

Previous literature reports have described the use of supported Pt nanoparticles over CeO_2 as a reducing agent for cerium oxide [23, 28, 32]. In a previous study of our group [32], in situ X-Ray Absorption Near Edge Structure (XANES) measurements were employed during a reduction treatment under H_2 atmosphere at 500 °C on Pd/CeO_2, Au/CeO_2, $Au\text{-}Pd/CeO_2$ and $Au\text{-}Pt/CeO_2$ nanoparticles.The results showed that cerium oxide support exhibits a higher Ce(III) fraction than the corresponding cerium oxide without metallic nanoparticles. This was attributed to a charge transfer from the metallic nanoparticles to the cerium oxide support during the thermal treatment. In fact, it depends on the nature of the nanoparticle supported. For Cu/CeO_2 and Ni/CeO_2 nanoparticles, our group demonstrated that the charge transfer occurs in the opposite direction, that is, from the support to the nanoparticle [33, 34]. The direction of the charge transfer is ruled by the differences on the work function of the nanoparticles and support [35]. In another previous work of our group [28], Pt/CeO_2 nanoparticles were studied with Ambient Pressure X-ray Photoelectron Spectroscopy (AP-XPS) measurements at 0.13 mbar in H_2 or 0.13 mbar in O_2 at 350°C in the Ce 4d region.The results revealed the reversibility of the redox reaction in Pt/CeO_2 nanoparticles when exposed to H_2 and O_2 atmospheres at 350 °C . This phenomenon was attributed to the dissociation of H_2 at

the Pt surface and its migration to the CeO_2 surface, resulting in the formation of water and oxygen vacancies through the H_2 spillover effect. The effect is illustrated below:

$$2Pt + H_2 \rightarrow 2(Pt - H) \tag{1.2}$$

$$(Pt - H) + CeO_2 \rightarrow (CeO_2 - H) + Pt \tag{1.3}$$

$$CeO_2 - H \rightarrow Ce^{3+}OOH \tag{1.4}$$

$$2CeO_2 - H \rightarrow Ce_2^{3+}O_3\square + H_2O \tag{1.5}$$

Where $\square$ represents an oxygen vacancy, a catalytically active site for CO_2 adsorption.

Goguet et al. [23] conducted a study about the behavior of Pt/CeO_2 nanoparticles in the RWGS reaction. The catalytically active sites (oxygen vacancies) are formed through the H_2 spillover effect and they are dispersed around the Pt nanoparticles. There are two reaction pathways for the RWGS reaction:

1- In the main route (path "a" in Figure 1.5), CO_2 molecules are adsorbed onto the oxygen vacancies present at the cerium oxide surface. Subsequently, the molecules undergo dissociation, resulting in the formation of CO, which is then desorbed from the catalyst surface.

$$CO_2 + \square + Ce_2O_3 \rightarrow CO + 2CeO_2$$

2- In the secondary route (path "b" in Figure 1.5), the interaction between the CO_2 molecule and the oxygen vacancy leads to the formation of CO. The CO molecule then migrates to the Pt-CeO_2 interface, where it is desorbed due to the weak Pt-carbonyl interaction.

These pathways highlight the different mechanisms by which the RWGS reaction can occur on the Pt/CeO_2 catalyst, providing insight into the role of oxygen vacancies and the Pt-CeO_2 interface in the overall reaction process.

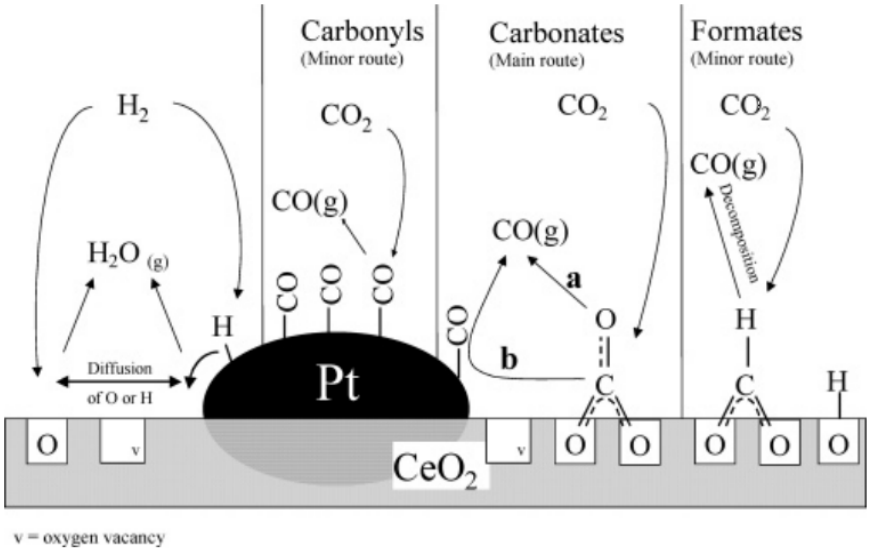

FIGURE 1.5. Schematic representation of the mechanism of the RWGS reaction in Pt/CeO_2 nanoparticles [23].

Both reaction routes involve cyclic reduction and oxidation of the CeO_2 support, enabling the feasibility of the reaction throughout the process. However, it is important to address potential factors that could diminish catalytic activity, such as carbon deposition and sintering of the Pt nanoparticles [23].

At elevated temperatures, the sintering of Pt nanoparticles becomes more frequent, resulting in a decrease in the Pt surface area. This decrease, in turn, leads to a reduction in the number of catalytically active sites for H_2 spillover effect. [36]. Carbon deposition on supported metal catalysts refers to the undesired formation of carbonaceous species, commonly known as carbon deposition or coking, at the surface of the catalyst. This phenomenon can occur during various catalytic reactions, particularly those involving hydrocarbons. The presence of carbon deposits can significantly impact on the catalytic activity and selectivity of the catalyst, impairing its performance over time. The deposited carbon can strongly chemisorb as a monolayer or physically adsorb in multilayers, obstructing the access of reactants to metal

surface sites. In both scenarios, carbon deposition has the potential to completely deactivate a metal particle by either blocking the active sites or encapsulating the particle entirely [36]. Figure 1.6 illustrates the carbon deposition on a supported metal catalyst.

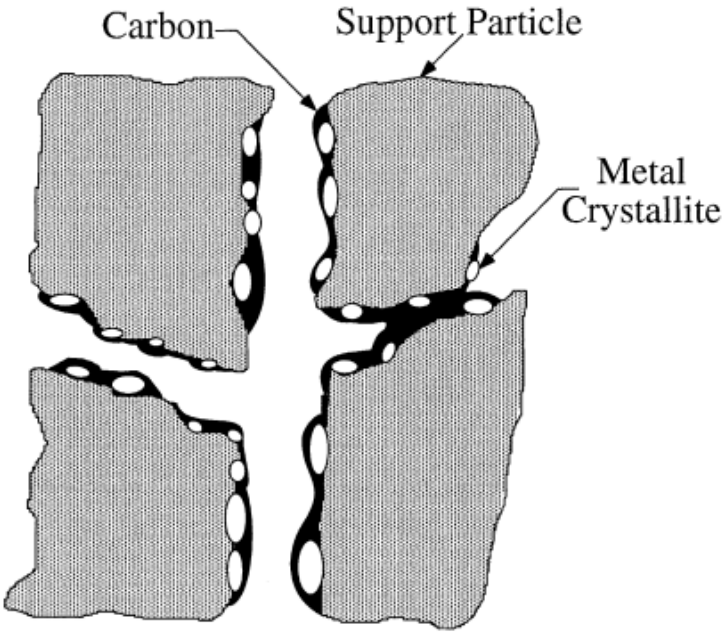

FIGURE 1.6. Conceptual model of carbon deposition on a supported metal catalyst [36].

Over the years, numerous efforts have been made to enhance the catalytic activity and selectivity of Pt/CeO_2 catalysts for the RWGS reaction. These attempts have involved various approaches, such as employing CeO_2 nanorods and nanofibers instead of nanoparticles, modifying the synthesis and supportation methods, variyng the amount of Pt deposition, and introducing dopants like Co and Fe into the Pt/CeO_2 catalyst [23, 21, 24, 25, 26, 37]. Nevertheless, two essential properties are desirable for all Pt/CeO_2 catalysts: (1) a high surface area and (2) the ability of CeO_2 to readily transition between its fully oxidized state (Ce(IV), CeO_2) and fully reduced state (Ce(III), Ce_2O_3).

In recent years, there have been significant advancements in the

development of modern Pt/CeO_2 catalysts for the RWGS reaction, as highlighted in Table 1.1. Noteworthy, Wang et al. [26] achieved a remarkable CO_2 conversion rate of 14% with 100% selectivity for the RWGS reaction at 300°C. However, it was observed that as the temperature increased, the CO_2 conversion also improved, but at the expense of significantly reduced selectivity for the RWGS reaction and the formation of byproducts such as methane. Another noteworthy study, conducted in 2023 by Nejadsalim et al. [25], focused on Pt-CeO_2/Mesoporous SiO_2 catalysts and reported a CO_2 conversion rate of 8.9% at 350°C, accompanied by 99% selectivity towards the production of CO. Besides the recent advances on the field, the negative consequences of global warming are advancing as well and it is urgent the development of new improved catalysts for this application.

1.4 Objectives

In this study, the main goal is to enhance the reactivity of Pt-CeO_2 nanoparticles towards CO formation in the RWGS reaction, at low temperatures. It is aimed to modify the properties of CeO_2, as this oxide plays an active role in the RWGS reaction. To achieve this, it will be employed superhydrophobic CeO_2 nanoparticles in Pt-CeO_2 catalysts. The concept behind using superhydrophobic CeO_2 nanoparticles is to minimize the adsorption of water molecules on the catalyst surface. It allows shifting the equilibrium of RWGS reaction towards the production of CO, thereby increasing the reactivity of the RWGS reaction.

Chapter 2

Experimental Techniques

In this chapter, the physical principles of the experimental techniques used throughout the work are addressed.

2.1 Rutherford Backscattering Spectrometry - RBS

Rutherford Backscattering Spectrometry (RBS) is an analytical technique used to identify and quantify the elements present in a sample. The technique consists on the incidence of a monoenergetic ion beam into a sample and the detection of the energy of the backscattered beam. The element identification is based on the energy lost in the backscattering event [38]. A simplified experimental setup for RBS is illustrated in Figure 2.1.

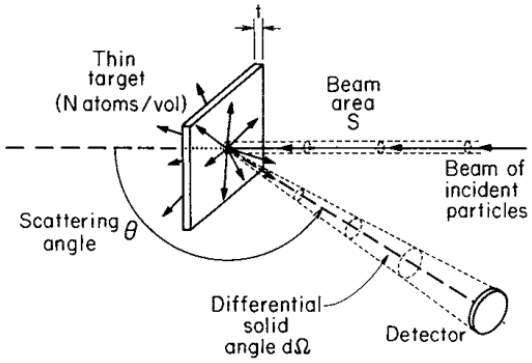

FIGURE 2.1. Simplified layout of a RBS experiment. [38]

The main parameters of the RBS experiment are the kinematic factor (K), scattering cross section, stopping power and straglling. The kinematic factor allows to identify qualitatively the elements present in the sample. It is given by the ratio between the energy of the ion just after (E) and the energy before the backscattering effect (E_0).

$$K = \frac{E}{E_0} \tag{2.1}$$

Therefore, the measurement of E of ions backscattered at the surface allows to identify the elements present in the sample since in this case the ion looses energy only due to the backscattering event. The kinematic factor is also given as a function of the atomic mass of the ion bean (M_1), the atomic mass of the sample (M_2) and the detection angle (θ) [38]:

$$K = \left[\frac{M_1 cos\theta + (M_2^2 - M_1^2 sen^2\theta)^{1/2}}{M_1 + M_2}\right]^2 \tag{2.2}$$

It is possible to show that the highest the scattering angle, the highest the differences on the K value, which is the reason for using high scattering angles in RBS analysis.

The scattering cross section (σ) is associated to the RBS quantitative property. The number of particles detected H is

$$H = QNt\left\langle\frac{d\sigma}{d\Omega}\right\rangle\Omega \tag{2.3}$$

where Q is the number of particles that hits the sample, N is the volumetric density, t is the target thickness and $\left\langle\frac{d\sigma}{d\Omega}\right\rangle$ is the scattering cross section over the solid angle Ω for the angle θ. For isotropic scattering, $\left\langle\frac{d\sigma}{d\Omega}\right\rangle$ is replaced by σ, therefore

$$H = QNt\sigma\Omega \tag{2.4}$$

$\frac{d\sigma}{d\Omega}$ is described by the eletrostatic repulsion from the nucleis given by the Rutherford formula [38]:

$$\frac{d\sigma}{d\Omega} = \left(\frac{Z_1 Z_2 e^2}{4E}\right) \frac{4}{sen^4\theta} \left[\frac{(1-((M_1/M_2)sen\theta)^2)^{1/2} + cos\theta}{(1-((M_1/M_2)sen\theta)^2)^{1/2}}\right]^2 \tag{2.5}$$

Where Z_1 and Z_2 are the atomic number from the ion and the target, respectively. Commonly $M_1 < M_2$ and θ The number of particles detected H is close to 180°, then this expression can be rewritten as

$$\frac{d\sigma}{d\Omega} = \left(\frac{Z_1 Z_2 e^2}{4E}\right) \frac{1}{sen^4(\theta)/2} \tag{2.6}$$

The stopping power (dE/dx) is the energy loss per length of ions as they penetrate into the target material, and it depends on the energy of the incident ion. The energy loss comes from both electron-electron and electron-nucleus interactions. In the case of particles backscattered close to the surface, (dE/dx) can be evaluated at E_0 (before backscattering) and KE_0 (after backscattering).

The straggling corresponds to the energy loss fluctuation as the ions interacts with the target. It is a statistical phenomena caused due to the discrete nature of the colisions. Therefore, it results in the widening of the ion bean energy as it penetrates into the sample.

Figure 2.2 illustrates a typical RBS spectrum obtained from a SiO_2 sample. In the RBS spectrum, each step corresponds to a different element present in the sample, and the height of each step is associated with the amount of that particular element.

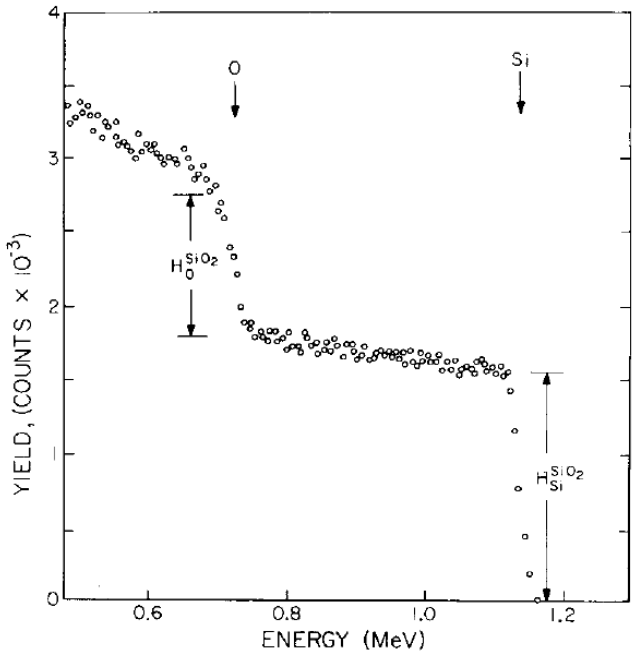

FIGURE 2.2. RBS spectrum for 2 MeV He ions incident on a sample of SiO_2 with elements identified [38].

RBS measurements commonly reveal the presence of multiple elements, such as C and N, which are frequently found as contaminants in various samples. However, in this specific spectrum, only the presence of Si and O was observed, most likely due to a previous treatment that effectively removed other elements from the sample.

2.2 Transmission Electron Microscopy - TEM

Transmission Electron Microscopy (TEM) is an experimental technique utilized in several fields of knowledge like physics, chemistry, and biology [39]. This technique enables the acquisition of high-resolution images at the atomic scale.

TEM is based on the incidence of an electron beam focused into a thin sample and the detection of the transmitted beam. It is similar

to the working principle of optical microscopy but using electrons as incident beam instead of photons. Consequently, it uses electromagnetic lenses instead of conventional lenses. Thanks to the small wavelength ($\lambda \leq 1$ nm) of electrons in the range of hundreds of keVs, electron microscopy offers significantly superior resolution compared to optical microscopy, which relies on photons with wavelength of hundreds of nanometers. Figure 2.3 illustrates the components of a transmission electron microscope: an electron gun, an anode, electromagnetic lenses, a fluorescent screen, and a CCD camera. The electromagnetic lenses consist of coils that control the focal point by adjusting the electric current. Electrons emitted from the electron gun are accelerated towards the anode and focused onto the sample using the electromagnetic lenses. The electron beam interacts with the sample through different phenomena, including secondary electron emission, backscattering, diffraction, and electron transmission [39]. Each of these phenomena can be utilized for different operation modes of the microscope. For this particular study, only the image mode was employed. In this mode, a portion of the electron beam passes through the sample, is refocused by a set of electromagnetic lenses, and then projected onto a fluorescent screen. The image projected onto the screen can be captured using a CCD camera. Figure 2.4 displays a typical TEM image, where dark regions result from less electrons transmitted through the sample. It occurs due to the electron backscattering upon collision with electron-dense regions or thicker parts of the sample, while lighter regions correspond to more electrons transmitted due to low electron density or thinner regions.

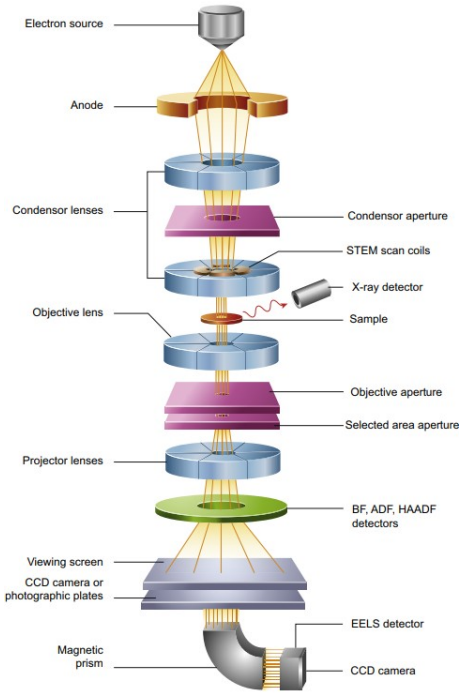

FIGURE 2.3. Simplified representation of a transmission electron microscope [40].

The sample preparation for TEM measurements depends on the type of sample to be analyzed [39]. Basically, the sample must be sufficiently thin for allowing electrons passing through it reaching the CCD camera, but not so thin that it becomes almost invisible to the electron beam. The term "thin" dependens on factors such as the electron energy and the atomic number of the material. However, as a general guideline, samples with thicknesses from 1 nm to 100 nm are typically employed [41]. In the case of nanoparticles in the powder form, the nanoparticles are initially diluted in some solvent and subsequently deposited onto a metallic grid coated with a thin carbon film. The liquid is then left to evaporate, leaving the nanoparticles adhered to the carbon film.

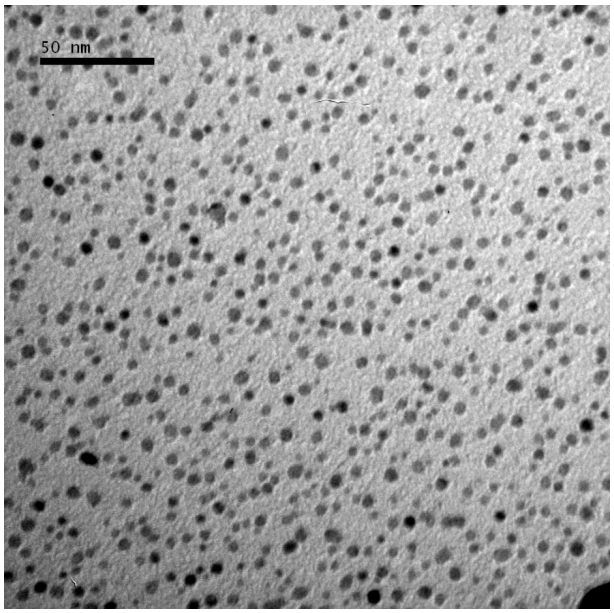

FIGURE 2.4. Typical TEM image of Pd nanoparticles. Image from an unpublished work of the group.

2.3 Synchrotron Radiation

Synchrotron radiation refers to electromagnetic radiation that is generated when charged particles with relativistic speed are deflected by a magnetic field perpendicular to its trajectory. This phenomenon can be observed in synchrotron laboratories, where electrons or positrons are accelerated to relativistic speeds within a ring-shaped structure with hundred meters of circumference. A typical synchrotron laboratory consists of five essential components [42], as illustrated in Figure 2.5:

1- Linear Accelerator (LINAC): This component generates the primary electron beam, typically in the range of hundreds of MeV.

2- Booster Ring: The electron beam from LINAC is further accelerated to reach the operational energy of the storage ring, typically of a few GeV.

3- Storage Ring: In this component, the electron beam circulates in

a closed path by utilizing bending magnets located at the intersections of straight sections. The magnetic field of these bending magnets is perpendicular to the trajectory of the electron beam. Due to the Lorentz force, the electron beam is deflected, emitting synchrotron radiation. Additionally, synchrotron radiation can also be produced using insertion devices like undulators or wigglers placed in the straight sections. Wigglers consist of a series of alternating magnets arranged to induce oscillations in the electron beam, resulting in the emission of synchrotron radiation during each oscillation, as depicted in Figure 2.6. To prevent collisions between the electron beam and any remaining particles, the storage ring operates under ultra-high vacuum conditions (around 10^{-9} mbar).

4- Radio Frequency (RF) Generator: This component transfers energy to the electron beam, compensating for energy losses caused by the emission of synchrotron radiation and collisions with residual gas molecules inside the storage ring.

5- Beamline: The synchrotron radiation generated can be used for different purposes (experimental techniques) in the beamlines.

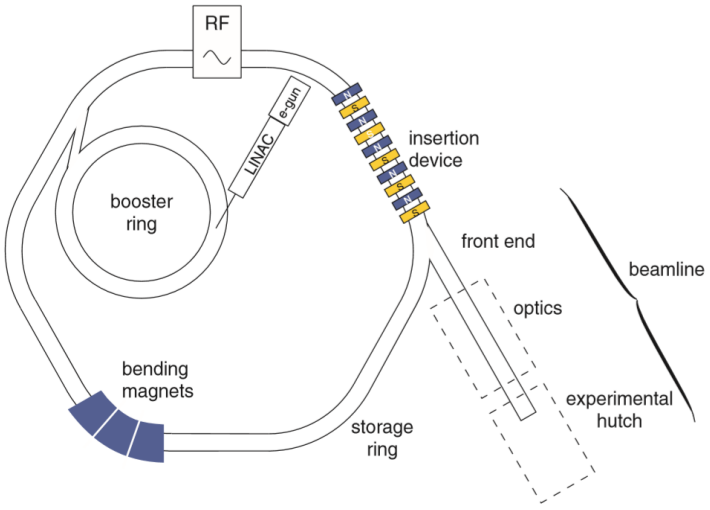

FIGURE 2.5. Simplified schematic representation of a synchrotron laboratory components [42]

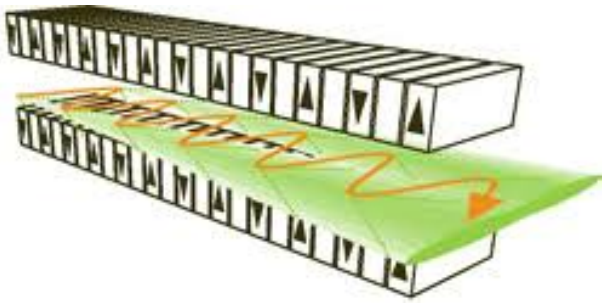

FIGURE 2.6. Schematic representation of a wiggler of a synchrotron laboratory.

Synchrotron radiation possesses several unique properties, including high brightness and a broad electromagnetic spectrum ranging from infrared to hard X-rays. This radiation has the ability to penetrate into the matter, allowing for the exploration of molecular and atomic properties. In fact, certain experimental techniques are only feasible due to the exceptionally high brightness achieved with synchrotron radiation.

2.4 X-ray Photoelectron Spectroscopy - XPS

X-ray Photoelectron Spectroscopy (XPS) is a widely used analytical technique that probes the surface region of a sample to gather information about the chemical state of its constituent elements [43]. This method involves directing a monoenergetic X-ray beam onto the surface and analyzing the kinetic energy of the emitted photoelectrons. The foundation of XPS lies in the photoelectric effect, which was formally explained by Albert Einstein in 1905 and earned him the Nobel Prize in Physics in 1921. The photoelectric effect, depicted in Figure 2.7(a), states that a photon with energy hν equal to or greater than the electron binding energy has a non-zero probability of exciting the electron, resulting in the ejection of a photoelectron with kinetic energy E_k, as described by Equation 2.7.

$$E_k = h\nu - E_b - \phi \tag{2.7}$$

where E_k is the kinetic energy of the photoelectron, E_b is the electron binding energy and ϕ is the analyser work function.

As a result of photoelectron emission from a core level, the excited atom subsequently relaxes by filling the resulting core hole with an electron from the valence level. This relaxation process releases energy through two primary mechanisms: x-ray fluorescence and Auger electron emission. In x-ray fluorescence, the relaxation process occurs through the emission of a photon with characteristic energy 2.7(b). However, this emitted photon is not detected in a XPS experiment. On the other hand, Auger electron emission 2.7(c) involves the emission of another electron (Auger electron) by the atom instead of a photon, which can be detected and is often used in XPS for qualitative and quantitative analysis.

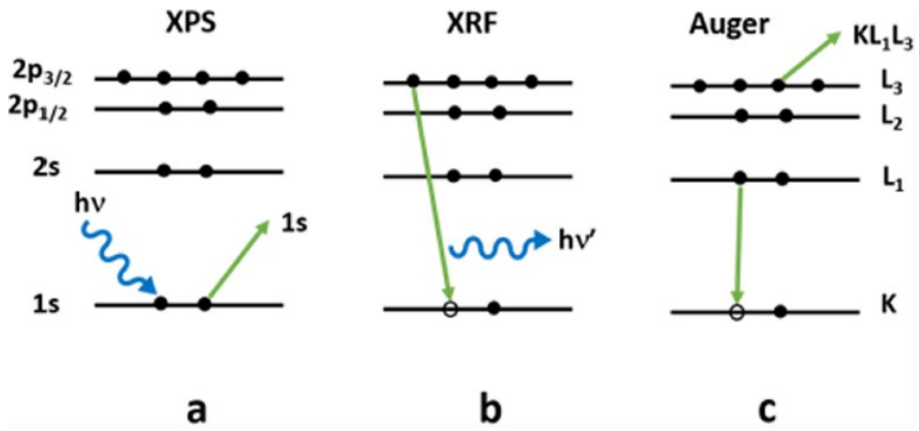

FIGURE 2.7. Schematic representation of the processes that result from x-ray incidence in a surface: (a) photoelectron emission, (b) x-ray fluorescence, and (c) electron Auger emission.[43].

The probed depth in XPS is determined by the Inelastic Mean Free Path (λ). The Inelastic Mean Free Path represents the average distance traveled by a photoelectron through a material before experiencing

any inelastic scattering. This distance is primarily dependent on the kinetic energy of the photoelectron and it remains relatively constant regardless of the material being investigated, as shown in Figure 2.8. Hence, the dependence of the inelastic mean free path with the kinetic energy is named universal curve. It is worth noting that almost all of the non inelastically scattered photoelectrons originate from a depth of approximately three times the Inelastic Mean Free Path (3λ).

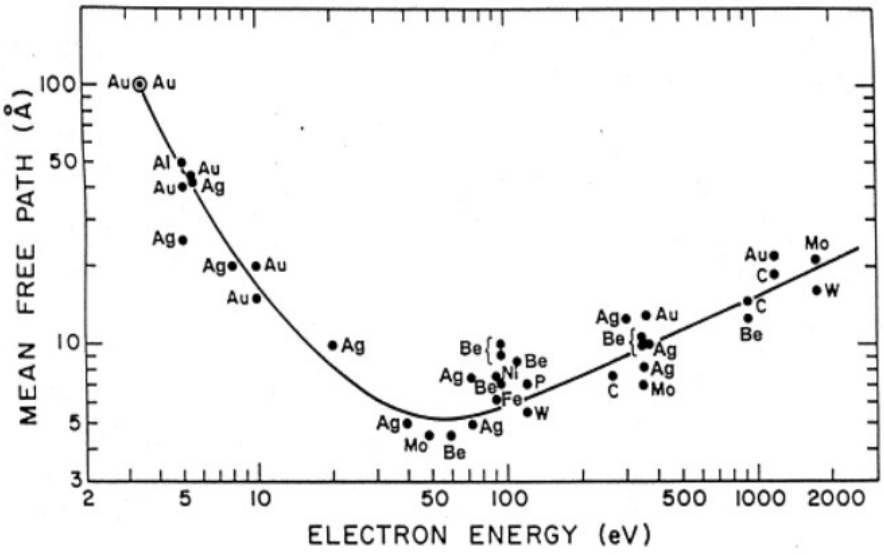

FIGURE 2.8. Universal inelastic mean free path as a function of the electron kinetic energy for different materials [44].

The XPS spectrum is constituted by the number of photoelectrons detected as a function of its kinetic or binding energy. Figure 2.9(b) illustrates a typical XPS spectrum. The peaks observed in the XPS spectrum correspond to the electrons that are not scattered inelastically (referred to as photoelectron A in Figure 2.9(a)). The photoelectrons inelastically scattered present smaller kinetic energy than the corresponding photoelectrons elastically scattered. It means that after the elastic peak there is a significant increase in the background, caused by the inelastic scattering of photoelectrons (depicted in orange in Figure 2.9. Each peak represents photoelectrons

coming from a specific electronic level of a specific chemical element. For example, Figure 2.9(b) demonstrates the XPS spectrum of PET (Poly(Ethylene Terephthalate)) and it exhibits peaks corresponding to C 1s and O 1s electronic levels, besides O Auger electrons.

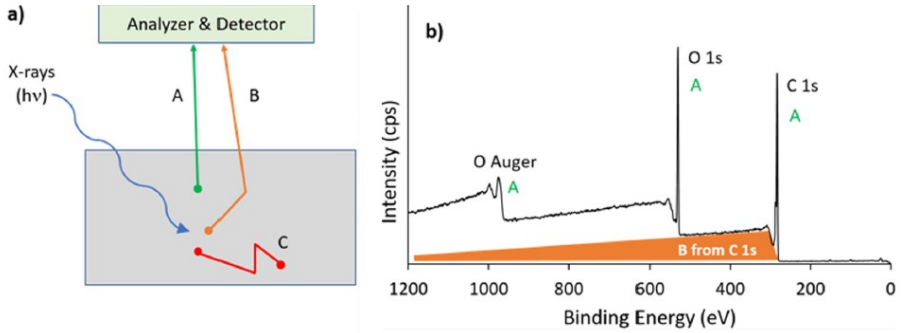

FIGURE 2.9. a) Possible trajectories of emitted photoelectrons and b) XPS spectrum of PET with the identification of the peaks and background [43].

Additionally, high-resolution measurements can be performed for specific electronic levels of the XPS spectrum, providing valuable information about the chemical environment at the surface of the sample. Figure 2.10 illustrates a high-resolution XPS spectrum in the C 1s region of a PET sample.

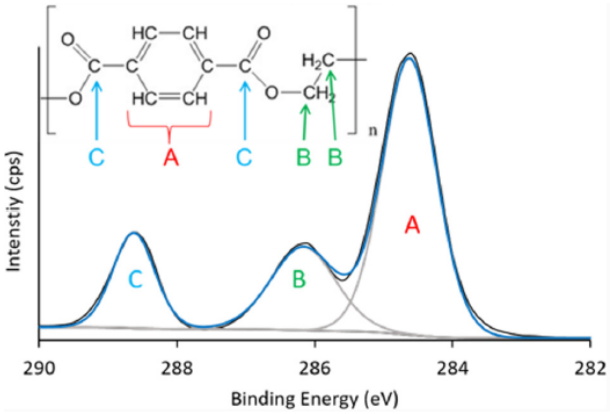

FIGURE 2.10. XPS high-resolution spectrum of the C 1s region of an PET with the chemical components identified [43].

The primary components of an XPS instrument include an x-ray source, sample stage, extraction lenses, analyzer, and detector, as depicted in Figure 2.11. The equipment operates inside an ultra-high vacuum (UHV) chamber, typically at pressures below 10^{-8} mbar. This is crucial for three main reasons: Firstly, it prevents photoelectrons from scattering with air molecules, strongly improving the signal to noise ratio of the measurements. Secondly, it helps to maintain the cleanliness of the sample surface, as XPS is a surface-sensitive technique. Finally, the analyzer operates only under UHV conditions. However, advancements in instrumentation have made it possible for spectrometers to be utilized $in\ situ$, even under relative high pressures and temperatures. This advanced technique is known as Ambient Pressure XPS (AP-XPS) measurements and represents the cutting-edge approach to surface characterization [45]. However, the availability of this technique is still quite limited around the world.

The typical setup for AP-XPS measurements in Synchrotron labs uses a thin membrane (usually made of Si_3N_4) or a differentially pumped system for protecting the vacuum in the beamline while allowing the X-ray beam to pass into the analysis chamber. The pressure ratio between the analysis chamber and the storage ring is maintained at about 10^9. Within the analysis chamber, the samples surface is positioned very close to a differentially-pumped aperture, which connects the electron analyzer to the chamber. This arrangement permits the sample to be surrounded by an ambient pressure nowadays up to 1 bar while conducting the measurements.

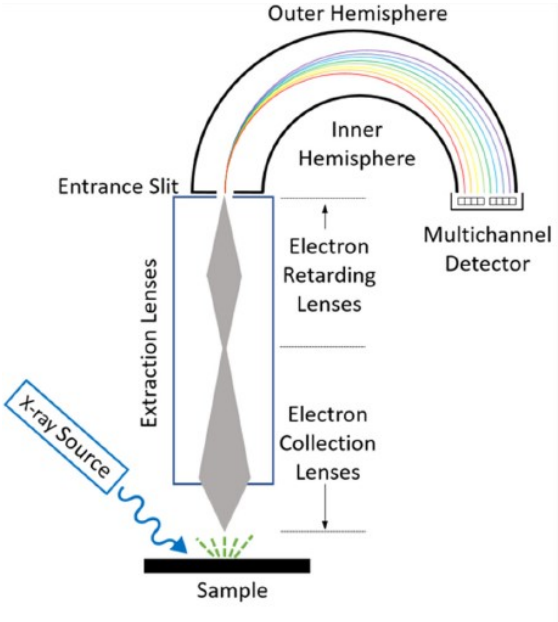

FIGURE 2.11. Schematic diagram showing the major components of an XPS instrument [43]

The x-ray source in XPS instruments is typically Al Kα (1486.3 eV) or Mg Kα (1253.6 eV). Many instruments are equipped with both sources, enabling the variation of photoelectron excitation energy. At the entrance of the analyzer, a series of electromagnetic lenses are positioned. In this region a voltage is applied aiming to retard the photoelectrons. Retarding the photoelectrons allows the user to define the energy of the photoelectrons before entering into the hemisphere region. The most commonly used analyzer in XPS is the concentric hemispherical analyzer, as depicted in Figure 2.11. It consists of two hemispheres, with the inner hemisphere maintained at a higher voltage than the outer hemisphere. Only photoelectrons with a specific energy (named pass energy) will be able to pass through the analyzer. Photoelectrons with lower energies will collide with the inner hemisphere, while those with higher energies will collide with the outer hemisphere. The voltage applied to the hemispheres can be adjusted by the user, allowing photoelectrons with different energies to pass through the analyzer and to reach the detector, which is typically

an electron multiplier. For high-resolution scans, small pass energies are typically employed to achieve better spectrum resolution, but with reduced photoelectron detection. Conversely, for survey scans, higher pass energies are often used to increase the efficiency of photoelectron detection, with less emphasis on resolution.

2.5 X-ray Absorption Spectroscopy - XAS

X-ray Absorption Spectroscopy (XAS) is an analytical technique employed to study the electronic state and local atomic order around a specific atom. It consists on illuminating a sample with a monochromatic X-ray beam while measuring the absorption coefficient as a function of the X-ray energy of the beam.

The X-ray absorption process is described by the Beer-Lambert's law, represented by Equation 2.8, which describes an exponential relationship between the intensity of the transmitted radiation and the sample thickness.

$$I(x, E) = I_0 \exp(-\mu(E)x) \tag{2.8}$$

where $I(x)$ is the intensity of the transmitted beam, I_0 is the incident intensity, x is the sample thickness and $\mu(E)$ is the absorption coeficient, which depends on the x-ray energy.

Figure 2.12 illustrates typical XAS spectra obtained at the Ce L_3 edge of a CeO_2 sample. The Ce L_3 edge corresponds to an electronic transition from the 2p to the 5d electronic level of the Ce atom. For a photon energy smaller than the binding energy of electrons in the Ce 2p electronic state, there is no photon absorption. However, as the incident photon energy reaches the same energy as the binding energy of this electronic state, there is a sudden increase in the absorption coefficient,

named absorption edge (E_b). When the photon energy exceeds E_b, the emitted photoelectrons have kinetic energy (E_k) greater than zero and they are scattered by the local atomic potential, which originates the oscillations in the absorption coefficient.

The XAS spectrum can be divided into two distinct energy regions: X-ray Absorption Near Edge Spectroscopy (XANES) and Extended X-Ray Absorption Fine Structure (EXAFS). The XANES region spans from the absorption edge, characterized by the abrupt increase in the absorption coefficient, to approximately 50 eV beyond the absorption edge. The XANES region provides information about the oxidation state and chemical environment of the absorbing atom. The EXAFS region begins in the end of the XANES region and it extends up to the end of the XAS spectrum. The EXAFS region provides information about the local atomic order around the absorbing atom, including the average distance between the absorbing atom and its neighbors, coordination number, and details about the thermal and structural disorder of the sample [46].

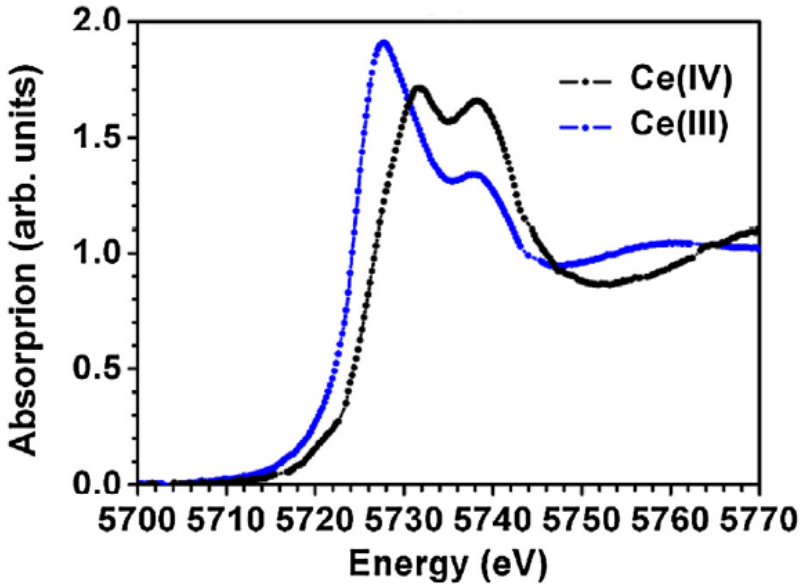

FIGURE 2.12. Typical normalized XAS spectra at the Ce L_3 edge. For the reduced Ce(III) state and the oxidized Ce(IV) state [47].

The quantitative analysis of the XANES region can be conducted through different approaches, including computational simulations. However, the most common one is the Linear Combination Analysis (LCA) [48]. The LCA method relies on fitting the experimental data using a linear combination of XANES standard spectra. In this way, it becomes possible to determine the relative proportions of different chemical compounds present in the sample.

Figure 2.13 illustrates the concept of the EXAFS oscillations. After being ejected from the absorbing atom, the photoelectron, manifested as a wave, has a nonzero probability of interacting with the remaining atoms in the sample. The neighboring atoms can backscatter the photoelectron wave, causing it to return to the absorbing atom. At this point, the backscattered photoelectron wave interacts with the original wave, resulting in either constructive or destructive interference. When constructive interference occurs, the X-ray absorption coefficient increases since the electron density at the absorbing atom also increases. In cases of destructive interference, the X-ray absorption coefficient decreases. The specific outcome depends on factors such as the distance between atoms, phase, and the wavelength of the photoelectron.

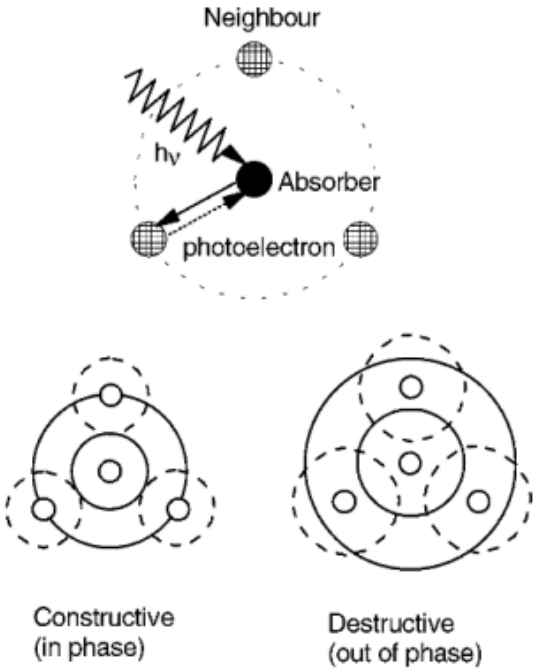

FIGURE 2.13. illustration of the photoelectron scattering process by neighbour atoms [49].

In Figure 2.14.a, the XAS spectrum at the Cu K edge for a Cu_0 sample is shown in blue, while the theoretical single atom contribution is displayed in red. Notice that the amplitude of the EXAFS oscillations constitutes only a small fraction of the overall X-ray absorption coefficient. In Figure 2.14.b, the isolated oscillations in the EXAFS region are presented, Figure 2.14.c displays the oscillatory data in real space, obtained by performing a Fourier Transform on the χ(k) oscillations [50]. The Fourier Transform is interpreted by considering the absorbing atom located at R=0Å, with each peak representing an atomic shell surrounding this atom.

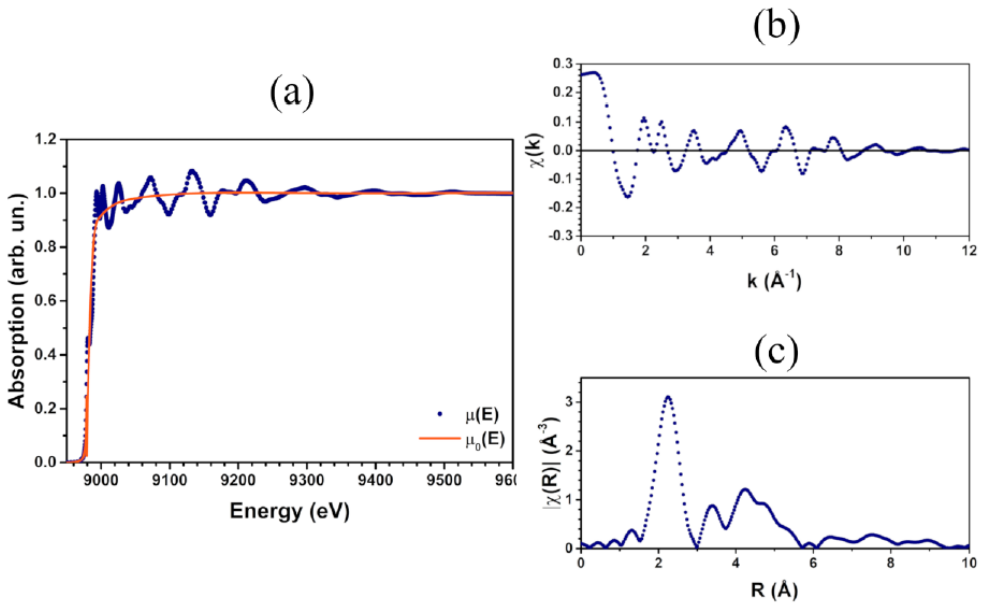

FIGURE 2.14. (a) XAS measurement at the Cu K edge of Cu, (b) the The respective EXAFS oscillations and (c) its the Fourier Transform [51].

The EXAFS oscillations are described by the equation:

$$\chi(k) = \sum_j = S_o^2 N_j e^{-2k^2\sigma_j^2} e^{-2\frac{R_j}{\lambda(k)}} \frac{f_j(k,\theta)}{kR_j^2} sin(2k_j R_j + \delta_j) \qquad (2.9)$$

where the sum occurs over the j atomic shells.

The amplitude reduction factor, denoted as S_o^2, is associated with the intrinsic processes of eletronic energy loss. The coordination number, N_j, represents the number of atoms of the same type located at approximately the same distance to the absorbing atom. The Debye-Waller factor, denoted as σ^2, incorporates the effects of thermal and structural atomic disorder and it is a convolution of both factors. This factor is directly influenced by the oscillation of atoms around their equilibrium positions and it becomes more significant at higher temperatures, contributing significantly to the EXAFS oscillations. The interatomic distance between the absorbing and scattering atoms is

represented by R_j. The mean free path, λ(k), characterizes the average distance traveled by the photoelectron in the material and it depends on the inelastic mean free path of the photoelectron, and the lenght associated to the lifetime of the hole produced in the photoemission process. It is typically a few angstroms in EXAFS measurements. The function $f_j(k, \theta)$ denotes the scattering amplitude of the photoelectron with a wave number k at an angle θ due to the neighboring atoms. The phase shift of the scattering process is represented by δ.

The analysis of the EXAFS oscillations is conducted with computational simulations. It is proposed an atomic cluster with a specific crystal structure to simulate the photoelectron scattering and then to calculate the $f_j(k, \theta)$ and δ_j factors. The theoretical calculation of these factors often involves the use of the muffin-tin potential. This potential, illustrated in Figure 2.15, consists of a Coulomb potential centered at the atomic positions, with a constant potential between the atoms. There are different packages used to calculate it but IFEFFIT is the most used one [52]. After this, the coordination number, distance between the absorbing and neighboring atoms, and Debye-Waller factor, are obtained from comparison between the simulated and measured data.

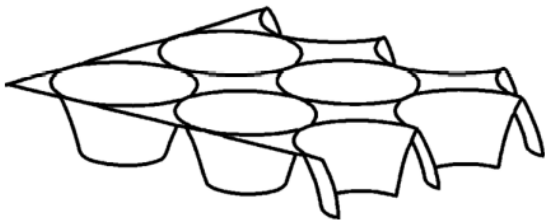

FIGURE 2.15. Two dimensional schematic representation of the muffin tin potential [46].

2.6 Small Angle X-ray Scattering - SAXS

Small-Angle X-ray Scattering (SAXS) is a technique employed to investigate the structural properties of a variety of materials, including nanoparticles with a wide range of size from few to hundred nanometers. This method involves directing a monochromatic X-ray beam, typically a Cu Kα radiation with a wavelength of 1.54 angstrons, onto a sample and analyzing the resulting scattering pattern at small angles, in relation to the incident direction, typically less than 5°.

The SAXS signal is typically represented as the intensity as a function of the scattering vector ($\vec{q} = \vec{k} - \vec{k'}$), where $\vec{k}$ is the incident wavevector and $\vec{k'}$ is the 2θ scattered wavevector. The modulus of the scattering vector can also be expressed in terms of the incident X-ray wavelength (λ) and the scattering angle (θ), as indicated by Equation 2.10.

$$q = \frac{4\pi}{\lambda} \sin\theta \tag{2.10}$$

The collective characteristics of the structures present in the sample can be described by the electronic density function ($\rho(r)$), which accounts for the spatial distribution of electrons. The scattering amplitude of an individual nanoparticle, often referred to as the form factor, can be obtained by the Fourier transform of the electronic density function:

$$f(q) = \int \rho(r')e^{-iq,r'}dr' \tag{2.11}$$

The intensity of the scattered X-rays, which is proportional to the differential cross section of scattering, is defined as the absolute squared value of the form factor

$$I(q) = |f(q)|^2 = \int \rho(r_1)\rho(r_2)e^{-iq(r_1-r_2)}dr_1dr_2 = \int \tilde{\rho}^2 e^{-iq,r}dr \qquad (2.12)$$

where $\tilde{\rho}$ is the convolution function and represents the density of electron pairs with a given relative distance. Depending on the material, a structure factor is also present but it will not be described in this work.

The analysis of the form factor with a fitting allows determining the size, shape, phase structure, roughness, fractal dimension and potentially even the electron density distribution of the scattering particles. This process involves finding a model (such as spherical, rod-like, monodisperse, etc.) that exhibits a scattering curve consistent with the experimental data. This procedure often requires multiple iterations and approximations, sometimes involving trial and error. It is a complex problem that necessitates careful adjustment and refinement to achieve a satisfactory agreement between the model and experimental results.

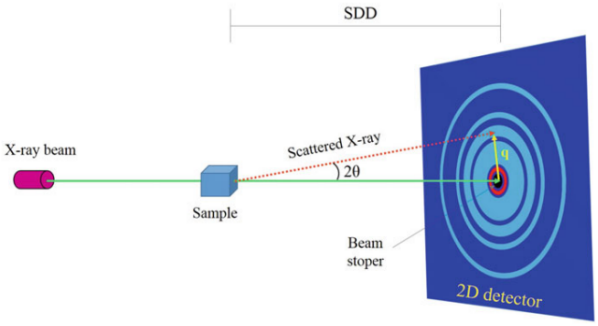

FIGURE 2.16. Basic schematic setup of a SAXS experiment [53].

Figure 2.16 depicts the fundamental schematic setup for SAXS, which includes an x-ray source, a sample holder, a beam stop, and a detector. The term SDD, shown in Figure 2.16, refers to the sample-to-detector distance. In the case of larger objects with sizes around 1 μm, the scattering pattern is predominantly observed at extremely small angles. Consequently, the ability of the SAXS equipment to detect and to analyze such scattering patterns is significantly influenced by the

physical properties of the SDD and the beam stop.

Bibliography

[1] Mikhaylov, A. et. al. Global climate change and greenhouse effect. Journal of Entrepreneurship and Sustainability Issues (2020)

[2] Kurane, I. The Effect of Global Warming on Infectious Diseases. Osong Public Health and Research Perspectives, 1(1), 4–9 (2010)

[3] Roy, P. et. al. Effects of climate change and sea-level rise on coastal habitat: Vulnerability assessment, adaptation strategies and policy recommendations. Journal of Environmental Management Volume 330, 117187 (2023)

[4] Liu, M. et. all. Causes of large projected increases in hurricane precipitation rates with global warming. Npj Climate and Atmospheric Science, 2(1) (2019)

[5] Lawrence, M. G. Promises and perils of the Paris Agreement. Science, 364(6443), 829–830 (2019).

[6] Rahman, F. A. et. al. Pollution to solution: Capture and sequestration of carbon dioxide (CO 2) and its utilization as a renewable energy source for a sustainable future. Renewable and Sustainable Energy Reviews, 71, 112–126 (2017)

[7] Thill, A. Development of highly promising NiO nanofoams for hydrogen storage application. Tese de Doutorado, Programa de Pós Graduação em Física pela UFRGS. (2023).

[8] Xie, Z. et. al. Metal-CO2 Batteries on the Road: CO2 from Contamination Gas to Energy Source. Advanced Materials, 29(15), 1605891 (2017)

[9] Ma, J.et. all. A short review of catalysis for CO2 conversion. Catalysis Today, 148(3-4), 221–231 (2009)

[10] Madejski, P., et. al. Methods and Techniques for CO2 Capture: Review of Potential Solutions and Applications in Modern Energy Technologies. Energies, 15, 887 (2022).

[11] Hus, M., et. al. Mechanism, kinetics and thermodynamics of carbon dioxide hydrogenation to methanol on $Cu/ZnAl_2O_4$ spinel-type heterogeneous catalysts. Applied Catalysis B: Environmental, 207, 267–278 (2017).

[12] GOGUET, A., et. al. Study of the origin of the deactivation of a Pt/CeO_2 catalyst during reverse water gas shift (RWGS) reaction. Journal of Catalysis, 226(2), 382–392 (2004).

[13] Kim, S. S., at. al. A study of the selectivity of the reverse water–gas-shift reaction over Pt/TiO_2 catalysts. Fuel Processing Technology, 108, 47–54 (2013).

[14] Jadhav, S. G., et. al. Kinetics of reverse water-gas shift reaction over Pt/Al_2O_3 catalyst. The Canadian Journal of Chemical Engineering, 94(1), 101–106 (2015).

[15] Chen, C.S., et. al. Study of reverse water gas shift reaction by TPD, TPR and CO2 hydrogenation over potassium-promoted Cu/SiO2 catalyst. Ap- plied Catalysis A: General, 238(1), 55–67 (2003)

[16] Kusama, H. et. al. CO2 hydrogenation reactivity and structure of Rh/SiO2 catalysts prepared from acetate, chloride and nitrate precursors. Applied Catalysis A: General, 205(1-2), 285–294 (2001).

[17] Dorner, R. W. et. al. Effects of ceria-doping on a CO2 hydrogenation iron–manganese catalyst. Catalysis Communications, 11(9), 816–819 (2010).

[18] Gogate, M. R. and Davis, R. J. Comparative study of CO and CO2 hydrogenation over supported Rh–Fe catalysts. Catalysis Communications, 11(10), 901–906 (2010).

[19] Lu, B. and Kawamoto, K. Preparation of monodispersed NiO particles in SBA-15, and its enhanced selectivity for reverse water gas shift reaction. Journal of Environmental Chemical Engineering, 1(3), 300–309 (2013).

[20] WANG, L. et. al. Effect of precipitants on Ni-CeO2 catalysts prepared by a co-precipitation method for the reverse water-gas shift reaction. Journal of Rare Earths, 31(10), 969–974 (2013).

[21] Porosoff, M. D. et. al. . Molybdenum Carbide as Alternative Catalysts to Precious Metals for Highly Selective Reduction of CO2to CO. Angewandte Chemie International Edition, 53(26), 6705–6709 (2014).

[22] Xu, W. et. al. The Carburization of Transition Metal Molybdates (MxMoO4, M = Cu, Ni or Co) and the Generation of Highly Active Metal/Carbide Catalysts for CO2 Hydrogenation. Catalysis Letters, 145(7), 1365–1373 (2015).

[23] Goguet, A., et. al. Spectrokinetic Investigation of Reverse Water-Gas- Shift Reaction Intermediates over a Pt/CeO2 Catalyst. The Journal of Phy- sical Chemistry B, 108(52), 20240–20246 (2004)

[24] Zhao, Z. et. al. Atomically dispersed Pt/CeO2 catalyst with superior CO selectivity in reverse water gas shift reaction. Applied Catalysis B: Environmental, 291, 120101 (2021).

[25] Nejadsalim, A. et. al. Core-Sheath Pt-CeO2/Mesoporous SiO2 Electrospun Nanofibers as Catalysts for the Reverse Water Gas Shift Reaction. Nanomaterials 13(3), 485 (2023).

[26] Wang, H. et. al. Synergistic Interactions of Neighboring Platinum and Iron Atoms Enhance Reverse Water–Gas Shift Reaction Performance. J. Am. Chem. Soc. 145, 4, 2264–2270 (2023).

[27] Daza, Y. A. and Kuhn, J. N. CO2 conversion by reverse water gas shift catalysis: comparison of catalysts, mechanisms and their consequences for CO2 conversion to liquid fuels. RSC Advances, 6(55), 49675–49691 (2016).

[28] Alayoglu, S., et. al. Pt-Mediated Reversible Reduction and Expansion of CeO2 in Pt Nanoparticle/Mesoporous CeO2 Catalyst: In Situ X-ray Spec- troscopy and Diffraction Studies under Redox (H2 and O2) Atmospheres. The Journal of Physical Chemistry C, 117(50), 26608–26616 (2013)

[29] Dai, B., et. al. Reduction of CO_2 to CO via reverse water-gas shift reaction over CeO2 catalyst. Korean Journal of Chemical Engineering, 35(2), 421–427 (2017)

[30] Trovarelli, A., et. al. Catalytic Properties of Ceria and CeO_2-Containing Materials. Catalysis Reviews, 38(4), 439–520 (1996)

[31] Khan, M. E., et. al. Ce3+-ion, Surface Oxygen Vacancy, and Visible Light-induced Photocatalytic Dye Degradation and Photocapacitive Perfor- mance of CeO2-Graphene Nanostructures. Scientific Reports, 7(1) (2017)

[32] Thill, A. S., et. al. Key Role Played by Metallic Nanoparticles on the Ceria Reduction. The Journal of Physical Chemistry C, 121(45), 25323–25332 (2017).

[33] Matte, L. P. et. al. Influence of the CeO2 Support on the Reduction Properties of Cu/CeO2 and Ni/CeO2 Nanoparticles. The Journal of Physical Chemistry C, 119(47), 26459–26470 (2015).

[34] Figueiredo, W. T. et. al. Understanding the Strong Metal-Support Interaction (SMSI) Effect in $CuxNi1 - x/CeO2$ (0 < x < 1) Nanoparticles for Enhanced Catalysis. ACS Applied Nano Materials (2019)

[35] Fu, Q. and Wagner, T. Interaction of nanostructured metal overlayers with oxide surfaces. Surface Science Reports, 62(11), 431–498 (2007).

[36] Bartholomew, C. H. Mechanisms of catalyst deactivation. Applied Catalysis A: General, 212(1-2), 17–60 (2001).

[37] Shen, D. et. al. Synergistic Pt-CeO2 interface boosting low temperature dry reforming of methane. Applied Catalysis B: Environmental 318 121809 (2022)

[38] Chu, W. k. et. al. Backscattering spectrometry. New York, Academic Press (1978)

[39] Williams, D. B., Carter, C. B.. Transmission Electron Microscopy, A Textbook for Material Science. Springer.

[40] Inkson, B.J. Materials Characterization Using Nondestructive Evaluation (NDE) Methods || Scanning electron microscopy (SEM) and transmission electron microscopy (TEM) for materials characterization. 17–43 (2016).

[41] Williams, D. B., Carter, C. B. Transmission electron microscopy. Springer (1996)

[42] Willmott, P., et. al. An Introduction to Synchrotron Radiation. John Wiley and Sons, Ltd (2011)

[43] Stevie, Fred A.; Donley, Carrie L. Introduction to x-ray photoelectron spectroscopy. Journal of Vacuum Science and Technology A, 38(6), 063204– (2020)

[44] Charles C. Chusuei, D.Wayne Goodman, in Encyclopedia of Physical Science and Technology (Third Edition), (2003)

[45] Frank Ogletree, D., et. al. Photoelectron spectroscopy under ambient pressure and temperature conditions. Nuclear Instruments and Methods in Physics Research Section A: Accelerators, Spectrometers, Detectors and Associated Equipment, 601(1-2), 151–160 (2009).

[46] J. Rehr and R. Albers. Theoretical Approaches to X-Ray Absorption Fine Structure. Revies of Modern Physics, vol. 3, pp. 621-654, (2000).

[47] Mea, G. B. D., et. al. Tuning the oxygen vacancy population of cerium oxide (CeO_{2-x}, $0 \leq x \leq 0{,}5$) nanoparticles. Applied Surface Science 422, 1102-1112 (2017).

[48] Benfatto, M., and Meneghini, C. A Close Look into the Low Energy Region of the XAS Spectra: The XANES Region. Synchrotron Radiation, 213–240. (2014)

[49] D. Koningsberger, et. al. XAFS spectroscopy: Fundamental Principles and Data Analysis. Topics in Catalysis, pp. 143-155, (2000).

[50] D. E. Sayers, et. al. New technique for investigating noncrystalline structures: Fourier analysis of the extended x-ray—absorption fine structure. Physical review letters, vol. 27, no. 18, p. 1204, (1971).

[51] Matte, P. L. Unraveling the influence of the CeO_{2-x} ($0 < x < 0.5$) properties on the reactivity of the Cu-CeO_{2-x} nanoparticles towards the CO oxidation reaction. Dissertação de Mestrado, Programa de Pós Graduação em Física. (2019).

[52] Ravel, B. and Newville, M. ATHENA, ARTEMIS, HEPHAESTUS: data analysis for X-ray absorption spectroscopy using IFEFFIT. Journal of Synchrotron Radiation, vol. 12, pp. 537-541, (2005).

[53] Londoño, O. M. et. al. Small-Angle X-Ray Scattering to Analyze the Morphological Properties of Nanoparticulated Systems. Handbook of Materials Characterization, 37–75 (2018).

[54] Kobelinski, D. R. B. Síntese sob demanda de mimético funcional da enzima superóxido dismutase em resposta a ambiente oxidante. Dissertação de Mestrado, Programa de Pós Graduação em Química. (2017).

[55] H.C. Yao, Y.Y. Yao. Ceria in automotive exhaust catalysts: i. oxygen storage. J.Catal. 86 254–265 (1984).

[56] Ziegler, J. F. et. al. SRIM – The stopping and range of ions in matter (2010). Nuclear Instruments and Methods in Physics Research Section B: Beam Interactions with Materials and Atoms, 268(11-12), 1818–1823 (2010).

[57] Schierbaum, K.-D. Ordered ultra-thin cerium oxide overlayers on Pt(111) single crystal surfaces studied by LEED and XPS. Surface Science, 399(1), 29–38 (1998).

[58] Thill, A. S., et. al. Key Role Played by Metallic Nanoparticles on the Ceria Reduction. The Journal of Physical Chemistry C, 121(45), 25323–25332 (2017).

[59] Pastor-Pérez, L., et. al. Effect of cold Ar plasma treatment on the catalytic performance of Pt/CeO_2 in water-gas shift reaction (WGS). Applied Catalysis B: Environmental, 225, 121–127 (2018).

[60] Campbell, C. T. CHEMISTRY: Oxygen Vacancies and Catalysis on Ceria Surfaces. Science, 309(5735), 713–714 (2005).

[61] Greczynski, G. and Hultman, L. The same chemical state of carbon gives rise to two peaks in X-ray photoelectron spectroscopy. Scientific Reports, 11(1) (2021).

[62] Matoliin, V. et. al. Methanol Adsorption and Decomposition on $Pt/CeO2(111)/Cu(111)$ Thin Film Model Catalyst. Langmuir, 26(16), 13333–13341 (2010).

[63] Björneholm, O. et. al. Overlayer structure from adsorbate and substrate core level binding energy shifts: CO, CCH3 and O on Pt(111). Surface Science, 315(1-2), L983–L989 (1994).

[64] Peuckert, M. XPS investigation of surface oxidation layers on a platinum electrode in alkaline solution. Electrochimica Acta, 29(10), 1315–1320 (1984).

[65] Cezar, J. C., et. al. Energy-dispersive X-ray absorption spectroscopy at LNLS: investigation on strongly correlated metal oxides. Journal of synchrotron radiation, 17(1):93–102, 2010.

[66] Koningsberger, D. C., et. al. X-Ray Absorption: Principles, Applications, Techniques of EXAFS, SEXAFS and XANES. R. Prins (1988).

[67] Ravel, B., Newville, M. Athena, Artemis, Hephaestus: data analysis for X-ray absorption spectroscopy using IFEFFIT. Journal of synchrotron radiation, 12(4):537–541 (2005).

[68] Takahashi, Y., et. al. Determination of the oxidation state of cerium in rocks by Ce L iii-edge X-ray absorption near-edge structure spectroscopy. Analytica Chimica Acta, 468(2):345–354 (2002).

[69] Wang, M. et. al. Oxygen vacancy generation and stabilization in CeO2-x by Cu-introduction with improved CO2 photocatalytic reduction activity. ACS Catalysis (2019).

[70] S. J. A. Figueroa, et. al. Upgrades to the XAFS2 beamline control system and to the endstation at the LNLS. Journal of Physics: Conference Series, vol. 712, no. 1, p. 012022, 92016).

[71] D. Koningsberger, et. al. XAFS spectroscopy: Fundamental Principles and Data Analysis, Topics in Catalysis, pp. 143-155 (2000).

[72] Figueiredo, F. R. A new proposal for avoiding sintering of nanoparticles in catalysis. Dissertação de Mestrado, Programa de Pós Graduação em Física pela UFRGS. (2021).

[73] Chen, J. Z., e. al. Strong Metal-Support Interaction (SMSI) of Pt/CeO2 and its Effect on Propane Dehydrogenation. Catalysis Today (2020).

[74] Abid, M. and Paul-Boncour, V. Pt/CeO2 catalysts in crotonaldehyde hydrogenation: Selectivity, metal particle size and SMSI states. Applied Catalysis A: General, 297(1), 48–59 (2006).

[75] WANG, L. et. al. Effect of precipitants on Ni-CeO2 catalysts prepared by a co-precipitation method for the reverse water-gas shift reaction. Journal of Rare Earths, 31(10), 969–974 (2013).

[76] Figueiredo, W. T. et. al. Determining the Surface Atomic Population in CuxNi1-x/CeO2 (0 < x < 1) Nanoparticles During Reverse Water-Gas Shift (RWGS) Reaction. The Journal of Physical Chemistry C (2020).

[77] Bernardi, F. et. al. Control of the surface atomic population of Rh 0.5 Pd 0.5 bimetallic nanoparticles supported on CeO 2. Catalysis Today, 260, 95–99 (2016).

[78] Ren, M. et. al. Electronic Metal-Support Interaction-Modified Structures and Catalytic Activity of CeOx Overlayers in CeOx/Ag Inverse Catalysts. Chem. - Eur. J. 25, 1597815982 (2019).